CrossMark

Stress-Induced Fracturing of Reservoir Rocks: Acoustic Monitoring and μCT Image Analysis

Srutarshi Pradhan[1] · Anna M. Stroisz[1] · Erling Fjær[1,2] · Jørn F. Stenebråten[1] ·
Hans K. Lund[1] · Eyvind F. Sønstebø[1]

Abstract Stress-induced fracturing in reservoir rocks is an important issue for the petroleum industry. While productivity can be enhanced by a controlled fracturing operation, it can trigger borehole instability problems by reactivating existing fractures/faults in a reservoir. However, safe fracturing can improve the quality of operations during CO_2 storage, geothermal installation and gas production at and from the reservoir rocks. Therefore, understanding the fracturing behavior of different types of reservoir rocks is a basic need for planning field operations toward these activities. In our study, stress-induced fracturing of rock samples has been monitored by acoustic emission (AE) and post-experiment computer tomography (CT) scans. We have used hollow cylinder cores of sandstones and chalks, which are representatives of reservoir rocks. The fracture-triggering stress has been measured for different rocks and compared with theoretical estimates. The population of AE events shows the location of main fracture arms which is in a good agreement with post-test CT image analysis, and the fracture patterns inside the samples are visualized through 3D image reconstructions. The amplitudes and energies of acoustic events clearly indicate initiation and propagation of the main fractures. Time evolution of the radial strain measured in the fracturing tests will later be compared to model predictions of fracture size.

1 Introduction

How to fracture reservoir rocks efficiently without damaging the well or the environment is a big challenge to the petroleum industry. This problem is also linked to the implementation of underground CO_2 storage and geothermal energy production scenarios. The fracture initiation mechanism and propagation dynamics (Fjær et al. 2008; Van Dam 1999) in porous rocks need to be analyzed and understood well for solving the problem and answering the calls—where does a fracture go? How does the fracture plane look like? How fast does the fracture move?

Micro-fractures of different sizes are produced during fluid injection in reservoir rocks. Usually, a sudden increase in fluid pressure generates a hydraulic fracture, but sometimes effective stress drop (due to stimulation or some other reasons) also plays a key role. In a porous reservoir, fluid pressure can rise due to heating, gas generation, mineralogical changes, communication with another high-pressure zone, or due to human activities associated with oil and gas exploration (Fjær et al. 2008; Van Dam 1999). So far, modeling of fracture initiation and growth (Fjær et al. 2008; Van Dam 1999; Chakrabarti and Benguigui 1997; Herrmann and Roux 1990) has not been very successful as it is often based on linear elastic fracture mechanics, with resulting predictions that fail to reproduce reality. In this work, we have studied fracturing in reservoir rocks through laboratory experiments (Stroisz et al. 2013; Pradhan et al. 2014). All the fracturing tests are done on hollow cylinder core samples under high injection pressure

✉ Srutarshi Pradhan
  srutarshi.pradhan@sintef.no

  Erling Fjær
  erling.fjaer@sintef.no

1 SINTEF Petroleum Research, Trondheim, Norway

2 Norwegian University of Science and Technology, Trondheim, Norway

🙆 Springer

with AE monitoring system that can locate the cracking events responsible for the fracturing process. We record AE data during the entire test until the main fracture opens up. Statistics of AE events—in terms of amplitude distribution and energy distribution—have been analyzed for all the rock types. We measure fracturing stress and radial strain of the rock sample during the test to compare those values with model predictions. Finally, the post-test CT images of the rock samples are taken and fracture patterns inside the rock samples are reconstructed and compared with AE analysis.

2 Stress-Induced Fracturing Test

2.1 Experimental Setup

We have used our Messtek and MTS load frames for this rock-fracturing study. High borehole pressures are obtained by injecting pressurized oil into a rubber tube fitted in the center of a hollow cylinder rock core. The tube prevents fluid to migrate into the sample during the test. The borehole pressure is enhanced gradually, upon 0.3 mm displacement of pump piston (equivalent to around 1 MPa pressure increase) between each step, until failure occurs. Constant oil confinement of 5 MPa is exerted on an impermeable sleeve during the entire test. This tightens the sleeve around the sample, adjusting the chain (attached around the middle part of the sample) for radial strain measurements and improving the pinducers–sample contacts. A symmetrically distributed push-in type of inserts are used to fix the position of 9–12 pinducers (small AE sensors) at the circumference of the samples, at four levels along the length (see Fig. 1).

We record acoustic emission signals during the fracturing tests by our Vallen system, consisting of a multichannel AMSY-5 with AEP4 preamplifiers, sampling rate 10 MHz. The AE sensors are piezo-elements of 1.3 MHz center frequency and 3.5 mm diameter. Acoustic signals are elastic waves produced by sudden internal stress redistributions caused by changes in the rock's body. Such structural changes concern mainly crack opening and growth, dislocation movement, etc. The maximum AE activity is found in the close vicinity of the peak stress at which the main fracture opens up (see Fig. 2).

The types of rocks tested in this study, with mineralogy and selected properties, are listed in Table 1. The samples were prepared as hollow cylinder plugs of 51 mm outer diameter, 10.5 mm inner diameter, and 135 mm length, approximately. We used our rock-cutting machine for sample preparation and no fluid was used—we used just dry air. All samples were tested dry, after 48 h drying at 120 °C in a normal oven without any heating–cooling
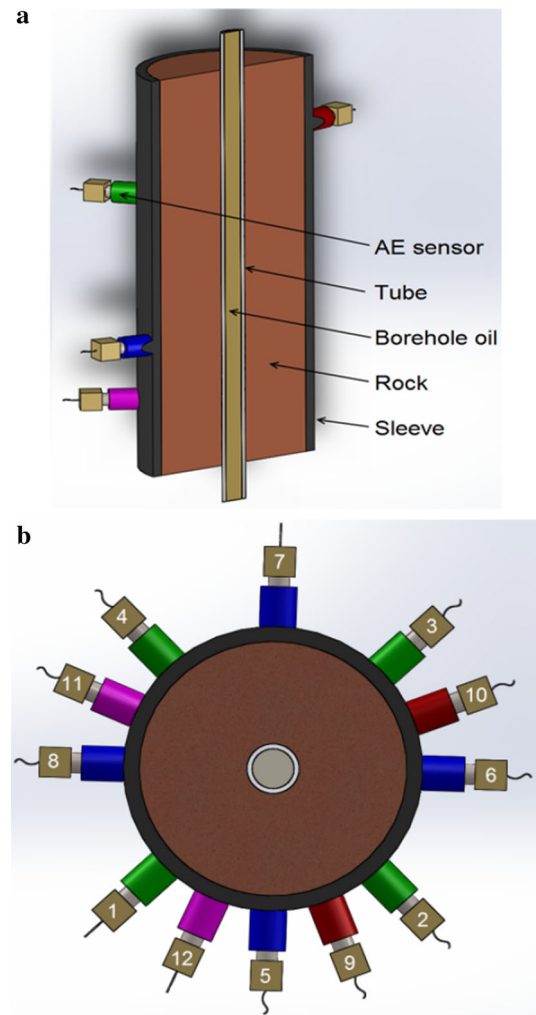

Fig. 1 Location of AE sensors in the setup shown in longitudinal (**a**) and cross- (**b**) sectional view. Sensors 1–4 (*green*) and 5–8 (*blue*) are positioned at 23 mm from the center to the top and bottom, respectively; sensors 9–10 (*red*) and 11–12 (*pink*) are at about 2/3 from the upper and lower edge of the sample, respectively. Adapted from Pradhan et al. (2014) with permission from ARMA

cycle. At least two samples for each rock type were examined—16 samples in total.

2.2 Test Procedure

The test procedure is as follows: first, the confining pressure and the borehole pressure are loaded to 2 and 1 MPa, respectively. There is no extra axial stress on the sample; the same confining pressure acts as axial pressure (hydrostatic condition). At this pressure condition, acoustic calibration is performed to check the activity of the individual acoustic sensors and adjust thresholds.

Next, the confining pressure is increased to 5 MPa, while the borehole pressure is kept unchanged at 1 MPa. This provides a well tightening of the sleeve around the
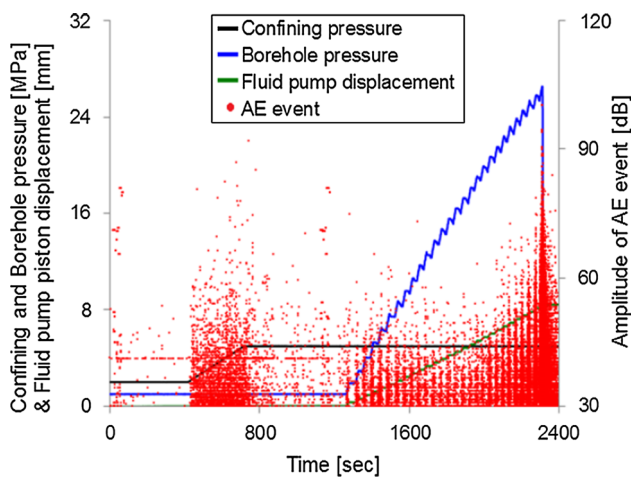
Fig. 2 Stress path and AE activity during the fracturing test. Confining pressure (*black*), borehole pressure (*blue*), piston displacement of the fluid pump (*green*) and AE events (*red points*). Data refer to a test on Saltwash North sandstone. Adapted from Pradhan et al. (2014) with permission from ARMA

sample, improving the contact between the acoustic sensors and the sample and adjusting the chain for radial strain measurements. The pressure condition is kept fixed until the sample becomes stabilized. Stabilization is achieved when AE activity is reduced significantly. The main part of the test is performed at constant confining pressure ($P_c = 5$ MPa) with stepwise increased borehole pressure. Borehole pressure increases until the main fracturing takes place, which is identified by the cumulative increase of the number of acoustic events and an abrupt drop of borehole pressure. An example of the stress path is shown in Fig. 2.

3 Experimental Results

3.1 Fracturing Stress

AE response on applied stress, as shown in Fig. 2, allows investigating the initiation and propagation of fractures. The fracturing process is recognized here by increased intensity and number of acoustic events. This increase proceeds gradually with increasing stress. The first large accumulation of events is related to the increase of the confining pressure. The average amplitude of these events is relatively low, which indicates that those signals originate from system noise (due to oil injection, and sleeve and sensor adjustment) or small structural changes rather than fracture generation. Further, a gradual increase of borehole pressure generates a series of higher-amplitude AE events at each pressure level. These events contribute to the fracture initiation process. The largest accumulation of events and the highest intensity is seen, however, in the

close vicinity of the peak pressure, where the main fracture opening takes place. The difference in the intensity of AE events before and close to peak pressure is particularly noticeable in an abrupt increase in energy. The amount of energy released during deformation depends on the amplitude and the duration of the acoustic events. That energy can be correlated to physical parameters such as mechanical fracture energy, rate and extent of damage development and deformation mechanisms.

The level of borehole pressure at which main fracture appears (peak borehole pressure P_b) differs for different rock types (see Table 2), but is fairly similar for the same rock type with less than 3 % relative difference between the samples.

The fracturing stress, determined from the experiments, is expected to be related to other strength parameters of the rock. Two strength parameters have been tested here—indirect tensile strength T_0 (from Brazilian tests) and unconfined compressive strength C_0 (from UCS test). The tests are conducted on the same rock samples as those used for the previous experiments in the Messtek frame. The results for all rock-strength parameters are given in Table 2. Note that the values are an average of all tested samples within a specific test method.

Based on linear elasticity and a tensile failure criterion (see for instance Fjær et al. 2008), fracturing should occur when the borehole pressure reaches the fracture initiation pressure P_{frac} given as

$$P_{frac} = \frac{1}{1+q^2}\left[2P_c + T_0\left(1 - q^2\right)\right], \qquad (1)$$

where q is the ratio between the inner and outer diameter of the hollow cylinder. Figure 3 shows the peak borehole pressure P_b plotted against P_{frac} for the data listed in Table 2. Clearly, P_b increases with T_0 similar to P_{frac} for both sandstone and chalk; however, P_b is significantly higher than P_{frac}, in particular for sandstone.

In a situation where there is no tube in the hole, the borehole fluid and its pressure will follow the fracture tip, and the force acting to open the fracture would increase, due to the increased attacking area. These effects tend to induce further growth. In our case on the other hand, the hole pressure is confined to the borehole because of the inner tube, so that the force acting to open up the fracture does not increase when the fracture grows, Instead, the growth of the fracture puts a distance between the attacking force and fracture tip, which tends to reduce the probability for further growth.

The figure also shows the maximum borehole pressure [$P_{max}(0)$] defined by the criterion that the outer force ($\propto P_c$ times outer diameter) equals the inner force ($\propto$ borehole pressure times inner diameter) minus the tensile resistance which is the tensile strength T_0 times the still intact area:

Table 1 Sample characteristics

Rock type	Properties
Berea	Formation: sandstone
	Composition: 80 % quartz, 12 % feldspar and rock fragments, 8 % clay
	Porosity: 18.9 %
	Density: 2.16 g/cm^3
	P-wave velocity: 2090 m/s
Castlegate	Formation: sandstone
	Composition: 70 % quartz, 30 % feldspar and rock fragments
	Porosity: 28.5 %
	Density: 1.92 g/cm^3
	P-wave velocity: 1830 m/s
Red Wildmoor	Formation: sandstone
	Composition: 42 % quartz, 47 % feldspar, 2 % other rock fragments, 9 % clay
	Porosity: 27 %
	Density: 1.91 g/cm^3
	P-wave velocity: 1690 m/s
Saltwash North	Formation: sandstone
	Composition: 86 % quartz, 9 % feldspar and rock fragments, 5 % clay
	Porosity: 21 %
	Density: 2.1 g/cm^3
	P-wave velocity: 1300 m/s
Saltwash South	Formation: sandstone
	Composition: 84 % quartz, 5 % feldspar and rock fragments, 11 % clay
	Porosity: 30 %
	Density: 1.8 g/cm^3
	P-wave velocity: 980 m/s
Mons	Formation: limestone (chalk)
	Composition: 99 % calcite (CaCO$_3$), 1 % quartz and pyrite inclusions
	Porosity: 44 %
	Density: 1.52 g/cm^3
	P-wave velocity: 2140 m/s
Lixhe	Formation: limestone (chalk)
	Composition: 99 % carbonate, 1 % silica and clinoptilolite
	Porosity: 42 %
	Density: 1.5 g/cm^3
	P-wave velocity: 2320 m/s

Table 2 Average peak borehole pressure (P_b) and rock strength parameters

Rock type	P_b (MPa)	C_0 (MPa)	E (GPa)	T_0 (MPa)
Berea	30.6	82.3	13.8	4.7
Castlegate	25.8	20.4	3.4	1.0
Red Wildmoor	25.5	19.3	3.4	0.9
Saltwash North	26.3	20.8	3.0	1.6
Saltwash South	20.2	1.9	0.3	0.2
Mons	20.0	13.3	4.9	1.7
Lixhe	19.7	10.0	4.7	1.0

$$P_{\max}(x) = \frac{1}{q}[P_c + T_0(1 - q - x)], \tag{2}$$

where x is the ratio between the fracture length and the outer radius of the hollow cylinder. As expected, all observations fall below this line. Note, however, that the maximum borehole pressure will be reduced once a fracture is initiated ($x > 0$). This suggests that the fracturing process is fairly abrupt for the rocks closest to the $P_{\max}$ line, while it is more gradual for the rocks that fall far from this line.
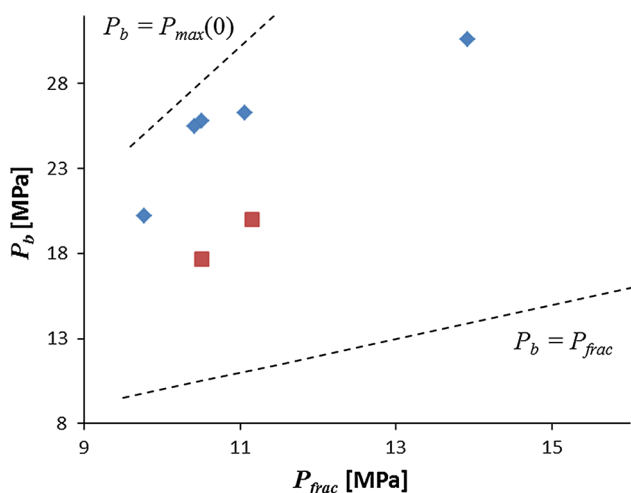
Fig. 3 The relation between observed peak borehole pressure and the fracture initiation pressure P_{frac} (Eq. 1). *Diamond symbols* represent data from sandstone samples and *square symbols* represent the data from chalk samples. The maximum borehole pressure $P_{frac}(0)$ is also shown

This implies that the peak borehole pressure is largely influenced by the test geometry, and that significant corrections have to be made to relate this parameter to fracture growth in a field situation. Alternative indications of fracture initiation and growth may also be considered.

3.2 Time Evolution of Radial Strain

The hold period at the initial part of the tests reveal a significant amount of creep, which may disturb the interpretation of the strain data. Creep can be evaluated using a model that combines a spring and dashpots elements (modified Burgers substance; see Fjær et al. 2008). This model takes into account transient creep and steady-state creep. According to this model, creep during loading can be represented mathematically as:

$$\varepsilon = a \times (1 - e^{-t/\tau}) + b \times t, \tag{3}$$

where a is the amplitude and τ is the time constant of the transient creep, and b is the steady state creep rate. Figure 4 a shows as an example how the model matches with the observations, while Fig. 4b shows how the radial strain develops when the delayed deformation is subtracted in accordance with this model. The creep-corrected data give a better description of the immediate response to borehole pressure changes. One can notice that the corrected radial strain vs. time plot shows a significant change of its slope around the fracturing point and the rate of AE events increases rapidly in that area (compare Figs. 2, 4). Creep estimation parameters obtained for all rock types are given in Table 3.
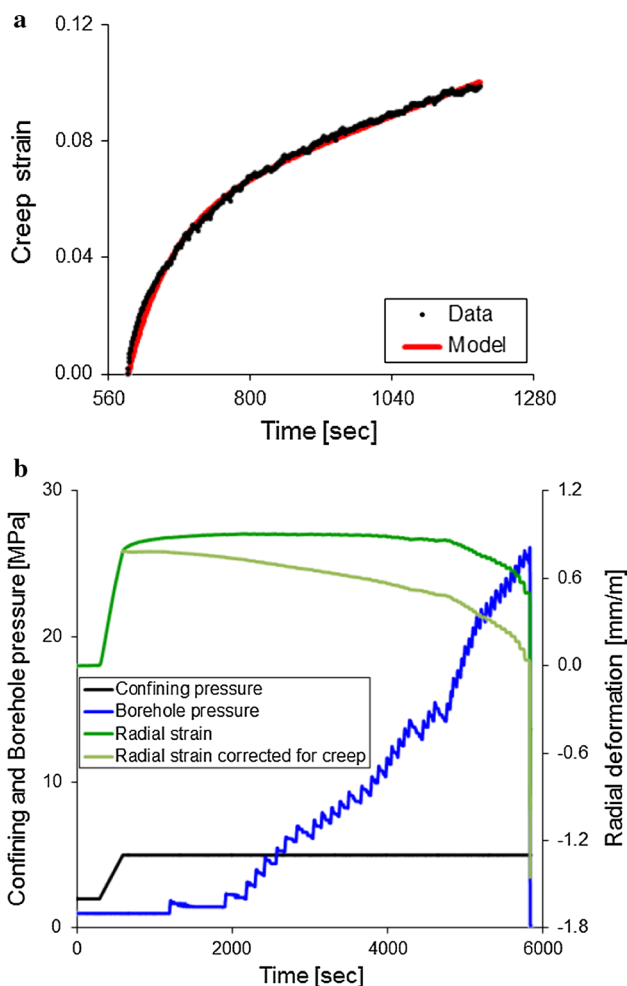

Fig. 4 Time evolution of radial creep during a fracturing test (**a**) and relevant radial strain correction for creep (**b**). The data refer to a test on Saltwash North sandstone

3.3 AE Event Locations and the Orientation of Main Fracture Arms

AE data were analyzed with the Vallen Visual AE software, which provides facilities necessary to extract the number of AE events, their amplitude and energy, and enables visualization of the results in the form of 2D and 3D event location graphs. We had not taken into account the acoustic velocity variations influenced by rock anisotropy and presence of micro-fractures; rather we assumed that the rock samples were isotropic. Therefore, a single acoustic velocity value was used for location estimation methods. During calibration, we have seen that the location estimation by our Vallen AE System remains within ±3 mm. Figure 5 compares the main fracture directions observed in the AE study with that of post-test imaging. The filtering functions in AE analysis enable specification of a particular portion of the data and reduction of

Table 3 Parameters describing the time evolution of the radial creep strain

Rock type	a	$\tau(s)$	$b(s^{-1})$
Barea	2.5e−2	62.5	4.9e−5
	1.5e−2	30.6	4.4e−5
Castlegate	4.0e−2	71.3	4.7e−5
	2.0e−2	20.4	2.2e−4
Red Wildmoor	2.8e−2	44.4	3.5e−5
	3.0e−2	46.8	1.1e−4
	3.6e−2	54.1	7.2e−5
Saltwash North	5.4e−2	72.1	7.9e−5
	4.4e−2	42.5	5.8e−5
Saltwash South	Large data scattering		
	Large data scattering		
Mons chalk	4.4e−3	12.1	4.2e−5
	9.8e−3	12.3	6.6e−5
Lixhe chalk	1.2e−2	23.4	2.1e−5
	2.1e−2	53.7	3.5e−5
	1.6e−2	22.9	1.4e−4

Fig. 5 Location of acoustic events indicates two symmetric fractures localized between AE sensors 6 and 8. This fracture is visible as clear core damage in the Castlegate sample

background noise. These options give information on the degree of damage in the sample and on how the damage process evolves (see Fig. 6) around the peak borehole pressure (P_b).

3.4 Statistics of AE Events

Analysis of acoustic emission (AE) signals during the fracturing tests can help understand the details of rock micro-fracturing and fracture propagation. AE studies utilize hypocenter mapping, event statistics and focal mechanism to investigate crack formation and propagation, damage precursors and failure modes of material/rock samples under compression or external loading. AE studies (Mogi 1962; Zang et al. 1996) for compression test on dry and wet sandstone reveal that micro-fracturing is actually controlled by the amount and distribution of weak minerals. A similar test on granite (Zang et al. 2000) has identified a zone of distributed micro-cracks (process zone) around the tip of propagating fractures and the recorded data show that the density of micro-cracks and amount of AE increase while approaching the main fracture. Another AE study on sandstone under hydrostatic and triaxial loading conditions (Fortin et al. 2006) confirms the formation of compaction bands during the fracture process. In case of fracturing in composite materials under external stress, AE bursts follow universal power law statistics that has been observed in numerical models (Pradhan et al.
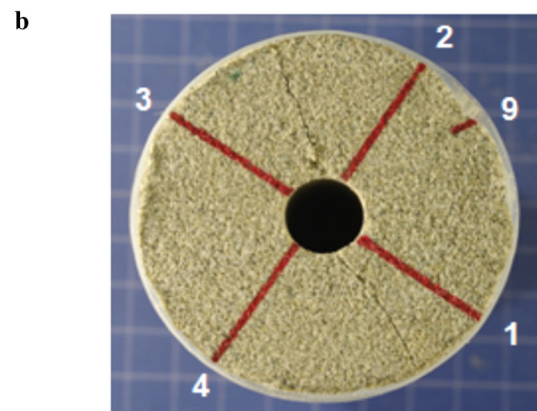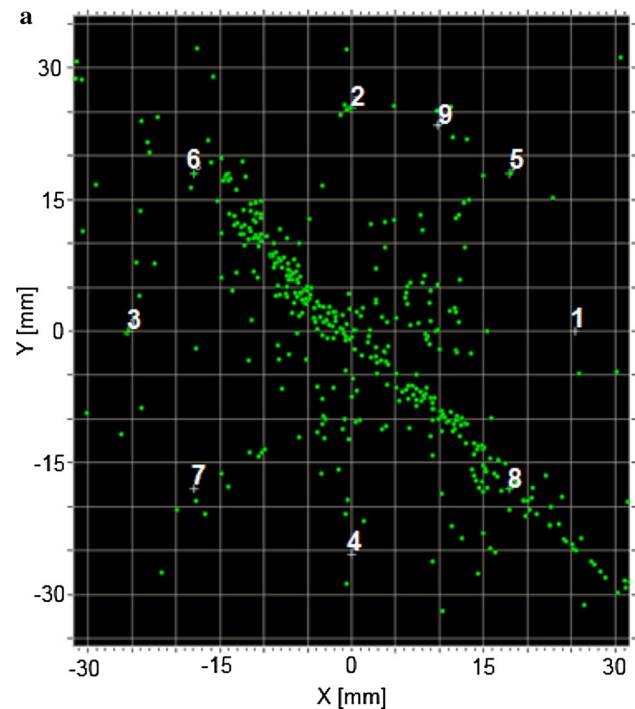
2005) and explained/confirmed by theoretical calculations (Pradhan et al. 2010).

During the entire fracturing test, we recorded AE events (Fig. 7). In all the cases, the event rate increases as we approach the final fracturing point. This feature is quite common in all the fracture models (Chakrabarti and Benguigui 1997; Herrmann and Roux 1990).

We have studied the statistics of AE amplitudes and energies recorded (Fig. 7) at different AE receiver channels (CH) of the Vallen AE monitoring system. Two examples (one for sandstone and the other for chalk) of the statistical distributions are shown in Figs. 8 and 9.
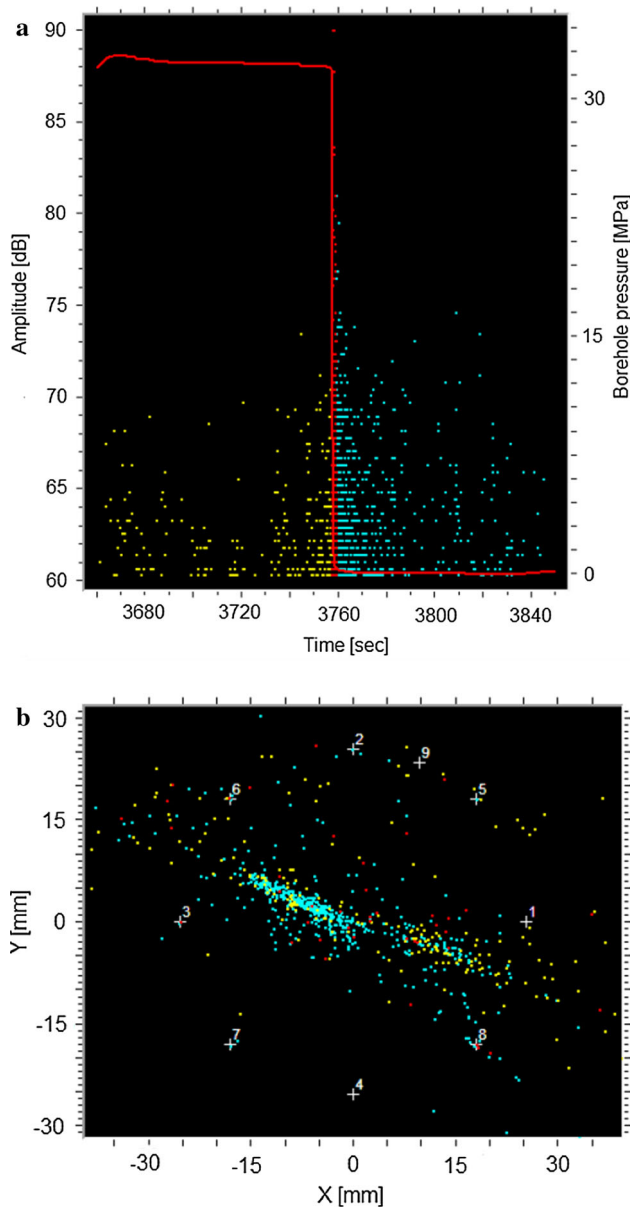
Fig. 6 AE analysis near the fracturing point: AE event amplitude near the fracturing point (*above*) and AE event locations (*below*). *Different colors* indicate the occurrence time: *yellow* (before P_b), *blue* (after P_b) and *red* (at the P_b)

It seems that the AE amplitudes follow an exponential distribution

$$P(A) \sim e^{-A/\alpha}, \tag{4}$$

and the AE energies follow a power law distribution

$$C(E) \sim E^{-\beta} \tag{5}$$

for all the rock types. But the values of α and β differ from rock type to rock type. We present these exponents values in a table below (Table 4).
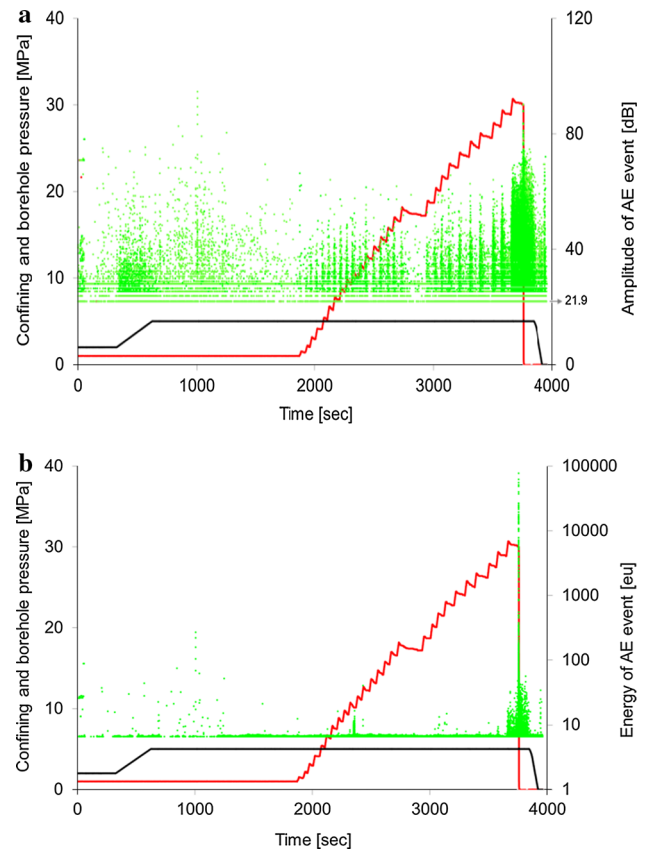

Fig. 7 Relation between stress increment and amplitude of AE events (**a**) and energy of AE events (**b**). A *green dot* represents a single AE event. The *black line* shows confining pressure and the *red line* shows borehole pressure. Only events with amplitude larger than a pre-set AE threshold (here: 21.9 dB) are included, to suppress noise. Sample—Berea sandstone. Adapted from Stroisz et al. (2013) with permission from ARMA

3.5 Post-Test μCT Image Analysis

Fractures generated during the test are, in most cases, clearly visible with bare eyes. However, for investigation of the internal fracture pattern, micro-CT imaging, with scans every 25 μm, was performed. Figure 10 shows the 2D and 3D image reconstruction for all the rock samples. Both figures show clearly the fracture patterns and their spatial change. All investigated sandstones seem to fracture in a similar way—with two fairly symmetric fractures around the borehole (see Fig. 10). These fractures are mainly restricted to one plane; an exception is the Berea sample where propagation of one fracture changes direction of about 30°. Contrary to sandstones, Mons chalk has more complicated fracture patterns. Fractures of different sizes appear within the entire volume of chalk, both vertically and horizontally. Parts of them merge, creating a complex pattern in which most of the fracture openings
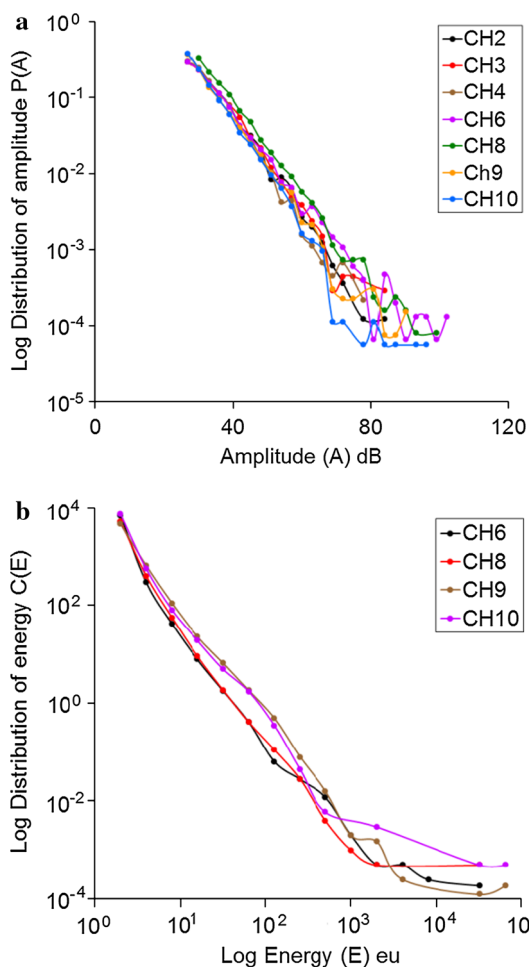
Fig. 8 AE amplitude (A) distribution and energy (E) distribution during the fracturing test on Saltwash North Sandstone sample. Adapted from Pradhan et al. (2014) with permission from ARMA
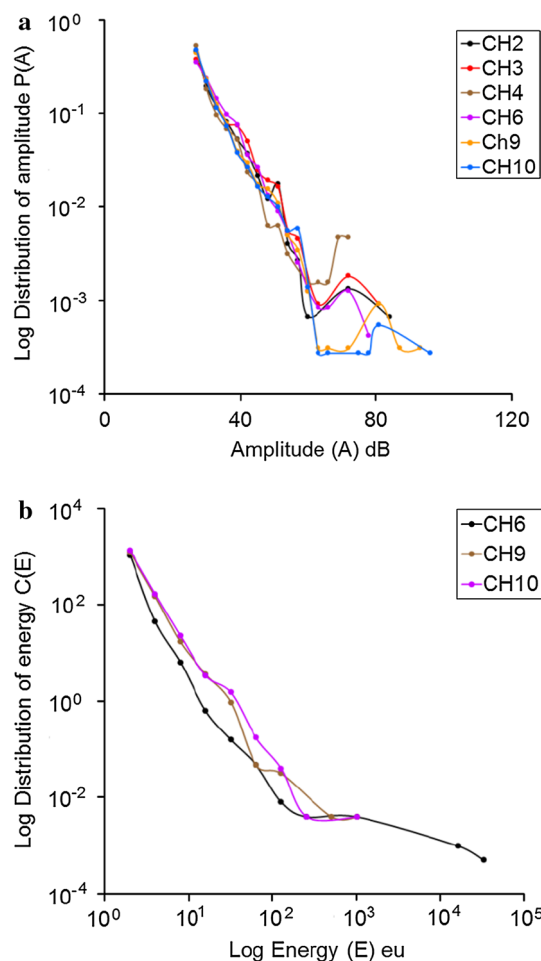

Fig. 9 AE amplitude (A) distribution and energy (E) distribution during the fracturing test on Lixhe chalk sample. Adapted from Pradhan et al. (2014) with permission from ARMA

appear closer to the external wall and less in the vicinity of the borehole.

### 3.6 Comparison Between AE Event Locations and μCT Image Analysis

On comparing CT images with the location of AE events (Fig. 11), it is clear that the AE fairly accurately retraces the fracture pattern. For all tested sandstones, most AE events are accumulated along two distinctive lines (Fig. 11a). These lines indicate the position of the major fracture openings. Moreover, 3D location graphs (Fig. 11b) show the vertical extension of the AE events. The events are predominantly distributed within one plane, which indicates a main fracture plane and is in accordance with reconstructed CT images (Fig. 10b). For Mons chalk, the location of the AE events is not as explicit—the AE events are randomly distributed within the entire sample. This is also in accordance with the reconstructed CT image.

Table 4 Distribution exponents for AE amplitude and energies for different rock types

Rock type	α	β
Barea	6	1.7
Castlegate	7	1.7
Red Wildmoor	6	1.6
Saltwash North	7	1.8
Saltwash South	6	1.8
Mons chalk	6	1.4
Lixhe chalk	5	1.9

Figure 11 presents results for the Berea sample. We choose it as an example to show how AE manages to retrace the fracture geometry. As shown in Fig. 10b, one of the fractures in the Berea sample deviates partly from the original direction ($\sim 30°$). This effect is also seen in the location of AE events (2D in particular, Fig. 11a) as spreading points. This spread is particularly pronounced around one of the lines (between sensor 1

Fig. 10 Fracture patterns visualized by CT imaging. Image reconstructions of all the rock samples are shown: **a** 2D reconstructions that include scans at different positions, at 1, 10, 40, 70, 100 and 130 mm, from the top of the specimen, and **b** 3D reconstructions
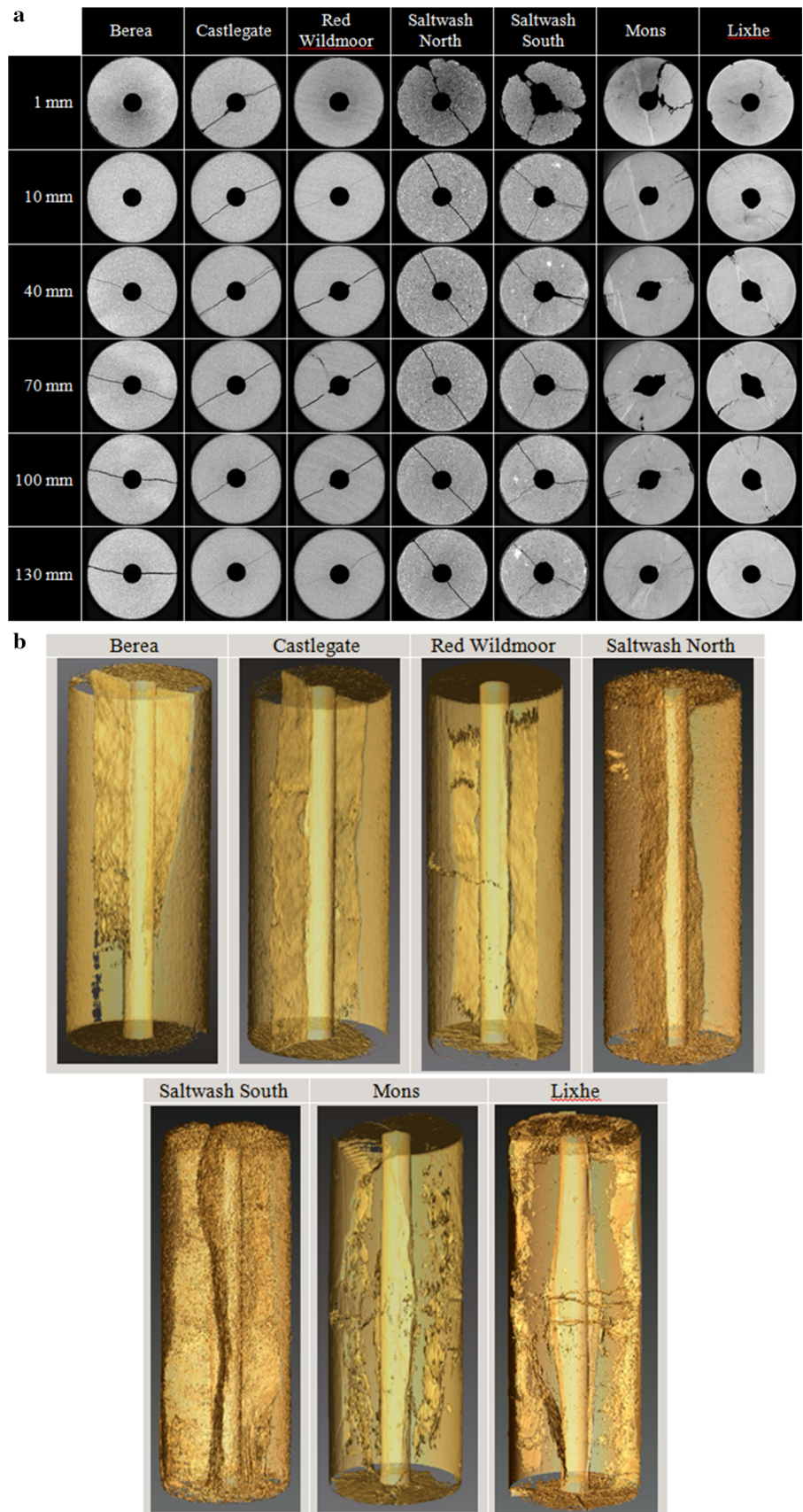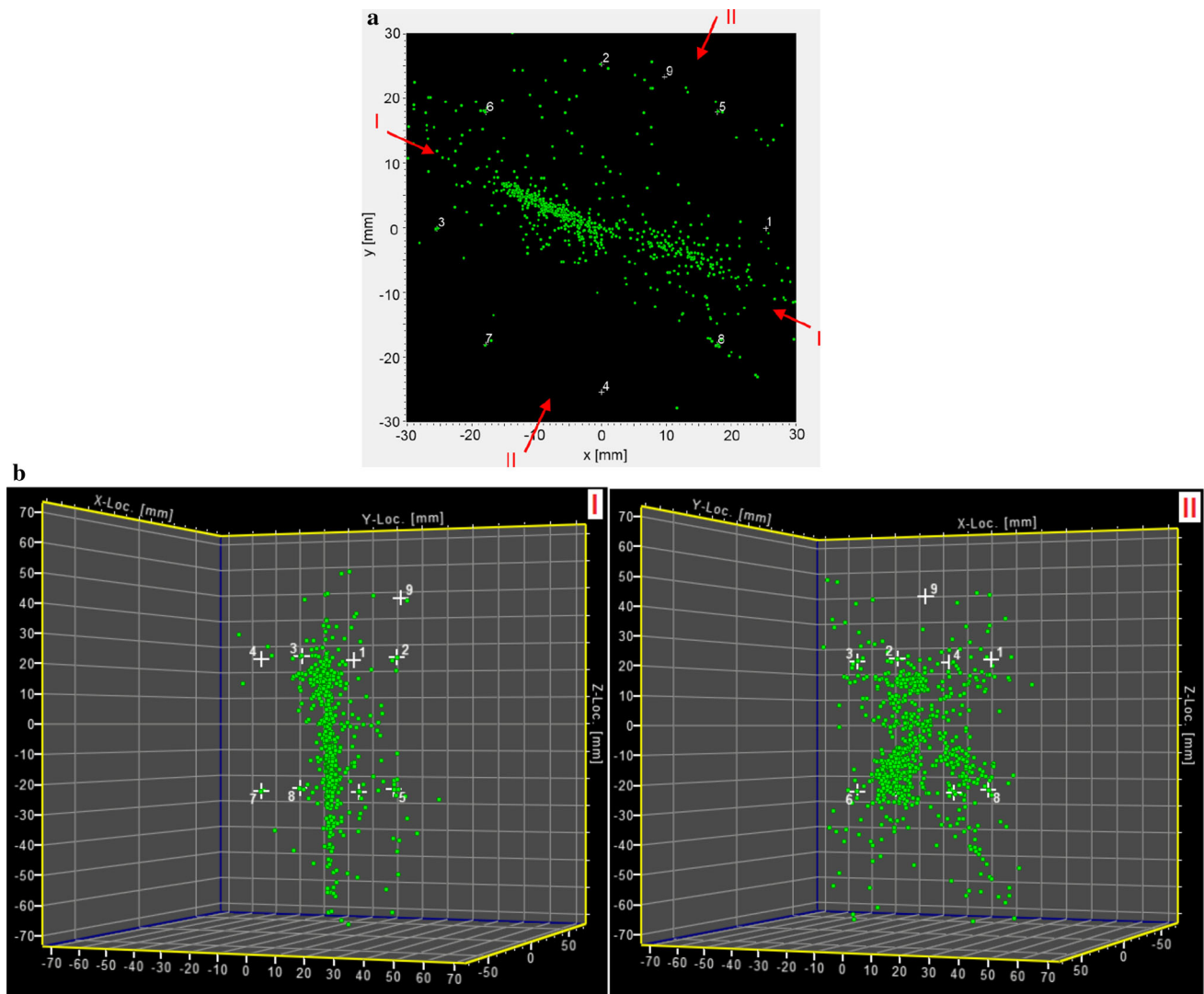
Fig. 11 Fracture pattern visualized via location of AE events. AE events, show in 2D (**a**) and 3D (**b**) location graph, have been restricted to the vicinity of fracture t ∈ (3500, 3900) s for Berea sandstone and filtered out with 60 dB. The labels *I* and *II* in figure **b** refers to the *line of sight* shown in figure (**a**). Adapted from Stroisz et al. (2013) with permission from ARMA

and 8), whose position is in accordance with the deviating fracture section. This is not seen for the other samples in which both fractures propagate along one plane.

Note that most of the AE events appear within the sample's boundary; only a small portion is located outside the specimen. This indicates that most of the recorded events come from structural changes, while only a part arises from noise generated by the apparatus or by AE echoes.

By separating the AE events according to their time of arrival, we should be able to reveal the progress of the fracturing process. So far, however, we have not been able to resolve the development of the fracturing process by this method.

4 Discussions and Future Research Directions

We have studied fracturing behavior of seven rock samples through laboratory tests and post-test AE and image analysis. Several important rock properties and rock-strength parameters have been measured (Tables 1, 2). The fracture-triggering stress values follow theoretical estimates with a small scaling correction factor—which comes from the finite geometry of the samples. Our observation on the evolution of radial strain follows model predictions—where creep effects have been taken into account. After subtracting the creep part, the corrected radial strain vs. time plot gives the actual response of the sample against increased borehole pressure. The slope of the plot changes rapidly around the fracturing point—which indicates

significant damage of the rock sample before complete fracturing. We have started analyzing this fracturing scenario through discrete element modeling (DEM) putting some exact input parameters such as tensile strength of the rocks, borehole pressure, element breaking criteria, etc. The model results match well with that of the laboratory tests qualitatively. We now calibrate the radial strain vs. time plot produced in DEM code against the same from the laboratory test for different types of rocks. The aim of this study is to find out the actual scaling factor (sample size dependent) that can give us the exact calibration of the plot—from which we can estimate the fracture length vs. radial deformation (or borehole pressure) for different rock types.

Statistical analysis of AE events gives the distribution exponents for AE amplitude and AE energies—these exponents differ from one rock type to another. High-energy distribution exponent (β values) for weak rocks (chalks) is a signature that high-energy events are less populated in weak samples, which is consistent with the observation that weak rocks do not produce big acoustic bursts.

The AE event location study shows the orientations and extends of the main fracture arms. It also shows the fracture plane inside the sample, which has been compared with CT image analysis. Through CT imaging, we have visualized the fracture planes, their width, inclination, etc.

The next phase of our laboratory test will be focused on performing the real hydraulic fracturing of rock samples using high viscous fluid. We have done some pre-tests in our MTS frame (without confining stress) and observed that the viscous silicon fluid can apply enough stress to fracture a sandstone sample (see Fig. 12).

5 Conclusions

In this work, we investigate different aspects of stress-induced fracturing of reservoir rocks through laboratory experiment, AE monitoring and post-test CT image analysis. At the peak borehole pressure (P_b), the main fracture opens up. Comparison of the P_b values with estimates from a classical fracture criterion shows that scaling corrections are needed to account for the effects of the finite sample size. All measured P_b values of different rocks appear to be within the rescaled theoretical limits. Creep during hold periods of borehole pressure is found to have a significant impact on the strain evolution and has to be corrected for to reveal the actual strain evolution. We notice that the intensity and energy of acoustic events increase sharply just before the peak borehole pressure, i.e., at the time when main fracture opens up. This observation has a potential to be used as a reliable alarm of upcoming

Fig. 12 Hydraulic fracturing of rocks using viscous silicon fluid: the high viscous silicon fluid entered inside the sample through the fractured surface

fracture opening or failure scenarios. The statistics of AE events follows exponential (AE amplitude) and power laws (AE energy), and the exponent values depend on the rock types. This indicates differences in the fracturing process between different rock types. Event locations revealed by AE studies show qualitative patterns and the orientation of main fractures in the sample. Post-test μCT image analyses produce 2D and 3D image reconstructions which reveal the fracture pattern after completion of the test. A good agreement between the observations from these two independent analyses proves the robustness of the results as well as confirms the usefulness of such post-test analysis to explore the details of the rock-fracturing scenario.

References

Chakrabarti BK, Benguigui L (1997) Statistical physics of fracture and breakdown in disordered systems. Oxford University Press, Oxford

Fjær E, Holt RM, Horsrud P, Raaen AM, Risnes R (2008) Petroleum related rock mechanics, 2nd edn. Elsevier, Amsterdam

Fortin J, Stanchits S, Dresen G, Gueguen Y (2006) Acoustic emission and velocities associated with the formation of compaction bands in sandstone. J Geophys Res 111:B10203

Herrmann HJ, Roux S (1990) Statistical models for the fracture of disordered media. Elsevier, Amsterdam

Mogi K (1962) Magnitude-frequency relation for elastic shocks accompanying fractures of various materials and some related problems in earthquakes. Bull Earthq Res Inst 40:831–853

Pradhan S, Hansen A, Hemmer PC (2005) Crossover behavior in burst avalanches: signature of imminent failure. Phys Rev Lett 95:125501

Pradhan S, Hansen A, Chakrabarti BK (2010) Failure processes in elastic fiber bundles. Rev Mod Phys 82:499

Pradhan S, Stroisz AM, Fjær E, Stenebråten J, Lund HK, Sønstebø EF, Roy S (2014) Fracturing tests on reservoir rocks: analysis of AE events and radial strain evolution. In: Proceedings of 48th U.S. Rock Mechanics/Geomechanics Symposium, ARMA-2014, Minneapolis, USA. Paper:14–7442

Stroisz AM, Fjær E, Pradhan S, Stenebråten J, Lund HK, Sønstebø EF (2013) Fracture initiation and propagation in reservoir rocks under high injection pressure. In: Proceedings of 47th U.S. Rock Mechanics/Geomechanics Symposium, ARMA-2013, San Francisco, USA. Paper:13–513

Van Dam DB (1999) The influence of inelastic rock behavior on hydraulic fracture geometry. Delft University Press, Delft

Zang A, Wagner CF, Dresen G (1996) Acoustic emission, microstructure, and damage model of dry and wet sandstone stressed to failure. J Geophys Res 101:17507

Zang A, Wagner CF, Stanchits S, Janssen C, Dresen G (2000) Fracture process zone in granite. J Geophys Res 105:23651